

Small-angle CMB temperature anisotropies induced by cosmic strings

Aurélien A. Fraisse*

Princeton University Observatory, Peyton Hall, Princeton, New Jersey 08544, USA

Christophe Ringeval†

*Theoretical and Mathematical Physics Group, Center for Particle Physics and Phenomenology,
Louvain University, 2 Chemin du Cyclotron, 1348 Louvain-la-Neuve, Belgium*

David N. Spergel‡

*Princeton University Observatory, Peyton Hall, Princeton, New Jersey 08544, USA
Princeton Center for Theoretical Physics, Princeton, New Jersey 08544, USA*

François R. Bouchet§

*Institut d'Astrophysique de Paris, UMR CNRS 7095,
Université Pierre et Marie Curie, 98bis boulevard Arago, 75014 Paris, France*
(Dated: August 25, 2008)

We use Nambu-Goto numerical simulations to compute the cosmic microwave background (CMB) temperature anisotropies induced at arcminute angular scales by a network of cosmic strings in a Friedmann-Lemaître-Robertson-Walker (FLRW) expanding universe. We generate 84 statistically independent maps on a 7.2° field of view, which we use to derive basic statistical estimators such as the one-point distribution and two-point correlation functions. At high multipoles, the mean angular power spectrum of string-induced CMB temperature anisotropies can be described by a power law slowly decaying as ℓ^{-p} , with $p = 0.889 (+0.001, -0.090)$ (including only systematic errors). Such a behavior suggests that a nonvanishing string contribution to the overall CMB anisotropies may become the dominant source of fluctuations at small angular scales. We therefore discuss how well the temperature gradient magnitude operator can trace strings in the context of a typical arcminute diffraction-limited experiment. Including both the thermal and nonlinear kinetic Sunyaev-Zel'dovich effects, the Ostriker-Vishniac effect, and the currently favored adiabatic primary anisotropies, we find that, on such a map, strings should be “eye visible,” with at least of order ten distinctive string features observable on a 7.2° gradient map, for tensions U down to $GU \simeq 2 \times 10^{-7}$ (in Planck units). This suggests that, with upcoming experiments such as the Atacama Cosmology Telescope (ACT), optimal non-Gaussian, string-devoted statistical estimators applied to small-angle CMB temperature or gradient maps may put stringent constraints on a possible cosmic string contribution to the CMB anisotropies.

PACS numbers: 98.80.Cq, 98.70.Vc

I. INTRODUCTION

The idea that all elementary-particle forces could simply be different manifestations of a single underlying force gained much strength after the successful elaboration of a unified renormalizable theory of electromagnetic and weak forces [1]. If the quest for the ultimate grand unified group of symmetries G has so far been unsuccessful, the mere idea of unification leads to strong theoretical predictions. In particular, if the particle physics interactions were unified at high energy, the expansion of the Universe should have triggered spontaneous breakdown of their symmetries [2]. Kibble showed that the induced phase transitions may form stable topological defects [3].

Cosmic strings are the linelike version of such primordial vacuum remnants. Their energy per unit length U is directly linked to the energy scale of the phase transition during which they were formed. Moreover, once formed, cosmic strings are stable and should still be present nowadays. Although an inflationary era occurring after a string-forming phase transition would dilute the defects enough to render them unobservable, defects formation at the end of inflation is a generic feature of particle physics motivated scenarios [4]. Motivated by the coincidence that strings formed at the grand unified theory (GUT) energy scale would induce density fluctuations with amplitude close to the observed amplitude of galaxy fluctuations, they were once considered as serious candidates to explain structure formation in our Universe [5]. However, the COBE data, associated to large-scale structure observations, already suggested that adiabatic fluctuations seeded galaxy formation [6], and the most recent high precision measurements of the cosmic microwave background (CMB) anisotropies leave little doubt that this conclusion is right [7]. Quite recently,

*Electronic address: fraisse@astro.princeton.edu

†Electronic address: ringeval@fyma.ucl.ac.be

‡Electronic address: dns@astro.princeton.edu

§Electronic address: bouchet@iap.fr

cosmic strings have also attracted the interest of the fundamental string theory community: the embedding of inflation in string theory may indeed produce another class of stringlike cosmological objects, dubbed “cosmic superstrings,” that could be fundamental or Dirichlet strings associated with extradimensional branes. Although of intrinsic Planckian-like energy density, their effective four-dimensional mass would be redshifted in presence of warped extra dimensions [8].

These theoretical considerations motivate the study of string-induced gravitational effects, such as lensing or gravitational wave emission [9, 10, 11, 12, 13, 14, 15, 16]. Using CMB and large-scale structure data, an upper limit to a potential cosmic defects contribution to the primordial inhomogeneity can be derived [17, 18]. The corresponding upper bound on the dimensionless energy scale GU (in Planck units) of local strings currently ranges from 2×10^{-7} to 10^{-6} and is a weak function of the model used to describe the string network. With the notable exception of Abelian string networks, whose induced CMB power spectrum has been recently obtained on the currently observable angular scales [19], many of the CMB analyses performed so far use analytical or semianalytical defect models which may or may not accurately mimic the cosmological evolution of a string network. These analytical approximations are often introduced to circumvent the difficulties associated with the highly nonlinear evolution of cosmic strings in an expanding universe. The theoretical understanding of cosmic string evolution in a Friedmann-Lemaître-Robertson-Walker (FLRW) universe is still an active field of research which has led to the development of numerical simulations incorporating all the defect dynamics [20, 21, 22, 23, 24, 25, 26, 27, 28]. A drawback is that they have a limited dynamic range in redshift making it impossible to directly compute the evolution of a network of strings from their formation to the present time.

These numerical limitations have motivated the search for simple signatures in the cosmological observables, such as straight temperature steps in the CMB temperature maps [29]. With the advent of new arcminute CMB experiments, such as the Arcminute Microkelvin Imager (AMI) [30], the South Pole Telescope (SPT) [31] or the Atacama Cosmology Telescope (ACT) [32], looking for strings directly into these maps may be promising. However, the efficiency of such searches would be greatly enhanced by the theoretical knowledge of the exact string patterns that may be imprinted in the microwave sky.

The goal of this paper is to generate realistic simulated CMB temperature maps that include the effect of cosmic strings on arcminute angular scales. For this purpose, we use high-resolution numerical simulations of Nambu-Goto strings based on an improved version of the Bennett and Bouchet code [22, 28]. As already mentioned, numerical simulations cannot probe a very wide range of redshifts. But as far as small angular scales are concerned, we can use the approach introduced by Bouchet [33] and compute the strings’ evolution starting

at the last scattering surface. Our method allowed the generation of 84 statistically independent maps, which we used to extract some basic statistical properties associated with the string patterns. Special attention has been paid to quantifying the systematic errors induced by the numerical initial conditions. We find that applying the gradient magnitude operator to our simulated CMB temperature maps leads to the reconstruction of the string shapes on the past light cone, which suggests that it may be of some help for direct searches. We then add Gaussian perturbations of inflationary origin and the Sunyaev-Zel’dovich (SZ) effects to our simulated maps. Convoluting the resulting maps with a diffraction-limited beam based on the specifications of the ACT experiment, we find that the gradient magnitude operator exhibits the strings’ signature down to $GU = 2 \times 10^{-7}$. While we defer the use of more sophisticated statistical estimators to a future paper, the clear non-Gaussian patterns showing up in the maps suggest that these estimators will significantly improve the current constraints on GU .

The paper is organized as follows. In Sec. II, we present our numerical simulations of cosmic string networks and the method used to simulate pure string-induced CMB temperature maps. Sec. III is devoted to a basic statistical analysis conducted on 84 simulated maps. We give the mean probability distribution function of the temperature fluctuations induced by strings and the corresponding mean angular power spectrum, with an estimation of the various associated errors. Some properties of the gradient magnitude of the string-induced temperature anisotropies are also discussed. In Sec. IV, we examine the observability of strings for an ACT-like experiment when the primary anisotropies, SZ effects, and the effect of beam smoothing are taken into account. The suitability of the gradient maps as strings tracer is reexamined in this context. We present our conclusions in Sec. V.

II. SIMULATED MAPS

A variety of methods have been used to compute the CMB anisotropies induced by cosmic strings. Many approaches rely on the use either of Green functions [34] or of unequal time correlators (UTC) [35], and all of them require the knowledge of the defect stress tensor evolution during the cosmological expansion. Because of the intrinsic nonlinear evolution of defect networks, this is usually achieved through numerical simulations in FLRW space-time [20, 21, 23, 24, 25], although simple analytical defect models [36, 37, 38, 39] have widely been used to circumvent the numerical limitations mentioned in Sec. I.

Computing the corresponding CMB angular power spectra requires only knowledge of the defect stress tensor two-point correlation functions. Since topological defects are active and incoherent sources of gravity perturbations, their two-point functions are generically nonvanishing at unequal times [40]. The UTC method relies on the scaling properties associated with an evolving cos-

mological string network to make this calculation easier. The network scaling properties indeed strongly restrict the UTC's functional form. They are then fit to numerical simulations and extrapolated to cosmological scales. This method has been successfully applied to derive the CMB and matter power spectra for a variety of topological defects [41, 42, 43, 44] and has recently been used with Abelian strings in Ref. [19].

Since we are interested in generating realistic maps, we need to go beyond computing the power spectrum. The two-point functions do not encode the non-Gaussian features induced by networks of defects in the CMB. We therefore use numerical simulations to capture the non-linear effects associated with the defect evolution, including non-Gaussianity. This approach has already been applied to constrain the energy breaking scale associated with various cosmic defects and to simulate full-sky CMB maps for Nambu-Goto strings [45, 46, 47, 48]. But due to the rather small expansion factor numerically achievable, such maps can only include stringy effects up to a finite redshift, typically $z \simeq 10^2$. The CMB anisotropies computed in this way are therefore only accurate on large angular scales. We avoid this limitation by stacking maps from different redshifts, an approach outlined in Ref. [33] and applied in Ref. [49]. While simulations with the observer outside of the numerical box are not well suited for a full-sky map reconstruction, they are quite useful for the small angular scales considered in this paper.

Denoting Θ_ℓ the ℓ th multipole moment of the temperature perturbation to photon distribution, the Boltzmann hierarchy in Fourier space can be recast into [50, 51]

$$\begin{aligned} \Theta_\ell = & \int_0^{\eta_0} g(\eta) e^{-k^2/k_D^2} (\bar{\Theta}_0 + \bar{\Phi}) j_\ell(k\Delta\eta) d\eta \\ & + \int_0^{\eta_0} \eta g(\eta) e^{-k^2/k_D^2} i \bar{v}_b j'_\ell(k\Delta\eta) d\eta \\ & + \int_0^{\eta_0} e^{-\tau} \left(\frac{d\Phi}{d\eta} + \frac{d\Psi}{d\eta} \right) j_\ell(k\Delta\eta) d\eta, \end{aligned} \quad (1)$$

where η_0 stands for the present conformal time, Ψ and Φ are the Bardeen potentials, $\Delta\eta = \eta_0 - \eta$, and v_b refers to the baryon velocity [52]. A bar has been used when the Silk damping term has been explicitly extracted from the perturbation variables [53]. The visibility function g is related to the optical depth τ through

$$g(\eta) \equiv -\frac{d\tau}{d\eta} e^{-\tau}, \quad (2)$$

and is strongly peaked around η_{lss} , the time of last scattering. As a result, the contribution of the first two integrals in Eq. (1), namely, the Sachs-Wolfe and Doppler terms, is only significant for $\eta \simeq \eta_{\text{lss}}$ [54]. Moreover, Silk damping exponentially washes these terms out for $k > k_D$, i.e., typically for $\ell \gtrsim 2000$. In presence of a cosmological string network, the Bardeen potentials Ψ and Φ in Eq. (1) are sourced by all the usual cosmological fluids, as well as by the strings. Following Ref. [5], if Ψ_{stg}

and Φ_{stg} refer to the perturbations that would be sourced by the strings alone, one can define $\Psi_m \equiv \Psi - \Psi_{\text{stg}}$ and $\Phi_m \equiv \Phi - \Phi_{\text{stg}}$. As only a minor string contribution appears to be compatible with the current CMB data [17, 18], $\Psi_{\text{stg}} \ll \Psi$, $\Phi_{\text{stg}} \ll \Phi$, and one may consider the stringy effects as a first order correction to the standard adiabatic cosmological perturbations. Although, in the presence of strings, the Bardeen potentials Ψ_m and Φ_m are coupled to Ψ and Φ through the perturbed Einstein equations, at leading order,

$$\Psi_m \simeq \Psi_{\text{coh}} \quad \text{and} \quad \Phi_m \simeq \Phi_{\text{coh}}, \quad (3)$$

where the index “coh” refers to the purely coherent Bardeen potentials of inflationary origin obtained without strings. Therefore, dropping the Sachs-Wolfe and Doppler terms in Eq. (1), one gets

$$\begin{aligned} \Theta_\ell \underset{k \gg 1}{\simeq} & \int_0^{\eta_0} e^{-\tau} (\dot{\Phi}_{\text{coh}} + \dot{\Psi}_{\text{coh}}) j_\ell(k\Delta\eta) d\eta \\ & + \int_0^{\eta_0} e^{-\tau} (\dot{\Phi}_{\text{stg}} + \dot{\Psi}_{\text{stg}}) j_\ell(k\Delta\eta) d\eta, \end{aligned} \quad (4)$$

where a dot denotes a derivative with respect to η . The first term represents the integrated Sachs-Wolfe effect for the standard cosmological fluids and would vanish in a purely matter-dominated universe. However, due to the recent domination of the cosmological constant and the existence of radiation residuals at the surface of last scattering, this term contributes significantly to the large angular scales, but is unimportant at small ones [50]. Moreover, as the Universe is optically thick before last scattering, Eq. (4) becomes

$$\Theta \simeq \int_{\eta_{\text{lss}}}^{\eta_0} e^{-\tau} (\dot{\Phi}_{\text{stg}} + \dot{\Psi}_{\text{stg}}) e^{-i\mathbf{k}\cdot\mathbf{x}_\gamma} d\eta, \quad (5)$$

where $\mathbf{x}_\gamma(\eta) \equiv \hat{\mathbf{n}} \Delta\eta$ is the photon path along the line of sight. At small angular scales, one may therefore expect the strings' signature in the CMB temperature fluctuations to be dominated by their integrated Sachs-Wolfe (ISW) effect from the last scattering surface. In the following, we use cosmic string numerical simulations and the so-called small-angle approximation to simulate CMB temperature maps according to Eq. (5).

A. Small-angle approximation

For Nambu-Goto strings, Φ_{stg} and Ψ_{stg} are solution of the perturbed Einstein equations sourced by the Nambu-Goto stress tensor. In the temporal gauge ($X^0 = \eta$), with $\alpha \equiv U/\sqrt{-g}$, it reads

$$T^{\mu\nu} = \alpha \int d\sigma \left(\epsilon \dot{X}^\mu \dot{X}^\nu - \frac{1}{\epsilon} X'^\mu X'^\nu \right) \delta^3(\mathbf{x} - \mathbf{X}), \quad (6)$$

where $\epsilon^2 \equiv \mathbf{X}'^2/(1 - \dot{\mathbf{X}}^2)$, U is the string energy per unit length entering the definition of the Nambu-Goto

action, and a prime denotes a derivative with respect to the string world sheet spacelike coordinate σ [55]. In the small-angle approximation, which is well suited for angles typically smaller than the Hubble angular size at the epoch of interest, Hindmarsh, Stebbins and Veeraraghavan showed that, in the case of Nambu-Goto strings, Eq. (5) can be simplified to [56, 57]

$$\Theta \simeq \frac{8\pi i GU}{\mathbf{l}^2} \int_{\mathbf{X} \cap \mathbf{x}_\gamma} (\mathbf{u} \cdot \mathbf{X}) e^{-i\mathbf{l} \cdot \mathbf{X}} e^{-\tau} \epsilon d\sigma. \quad (7)$$

The wave vector \mathbf{l} denotes the transverse component of \mathbf{k} with respect to the line of sight $\hat{\mathbf{n}}$, whereas, in the temporal gauge, \mathbf{u} encodes the string stress tensor distortions of the photon temperature and reads

$$\mathbf{u} = \dot{\mathbf{X}} - \frac{(\hat{\mathbf{n}} \cdot \mathbf{X}') \cdot \mathbf{X}'}{1 + \hat{\mathbf{n}} \cdot \dot{\mathbf{X}}}. \quad (8)$$

As can be seen in Eq. (7), only the strings that intercept the photon path can imprint their signature in the CMB temperature fluctuations. As a result, the knowledge of \mathbf{u} , and therefore of the string trajectories \mathbf{X} , is only required on our past light cone. In the context of string numerical simulations, the trajectories of all the strings are computed for all times. Therefore, to compute \mathbf{u} , one only needs to determine what parts of the string network intercept our past light cone at a given time. Equation (7) was also at the basis of the earliest string maps presented in Ref. [33]. However, our source terms in Eq. (8) are slightly different than the ones used in Refs. [33, 58] and include an additional longitudinal component with respect to the string trajectory [56]. As discussed in Ref. [57], this component encodes a logarithmic correction to the temperature fluctuations induced by the string curvature and may be significant for wiggly strings.

B. Cosmic string evolution

Since Eq. (5) involves an integration from the last scattering surface to the present time, we are left with simulating the cosmological evolution of a network of cosmic strings from $z \simeq 1100$ to $z \simeq 0$.

Our numerical simulations in FLRW space-time are based on an improved version of the Bennett and Bouchet Nambu-Goto cosmic string code [22, 28]. The runs are performed in a comoving box with periodic boundary conditions and whose volume has been scaled to unity. The scale factor is initially normalized to unity, while the horizon size d_{h_0} is a free parameter controlling the initial string energy within a horizon volume. During the computation, the comoving horizon size grows and the evolution is stopped before it fills the whole unit volume to avoid spurious effects coming from the boundary conditions. We use the Vachaspati-Vilenkin initial conditions for which the long strings path is essentially a random walk of correlation length ℓ_c , together with a random transverse velocity component of root mean squared

amplitude 0.1 [59]. The initial horizon size and velocity amplitude are chosen to minimize the relaxation time of the Vachaspati-Vilenkin string network toward its stable cosmological configuration. As mentioned before, the finite numerical box limits the range of scale factors during which the string evolution can be computed at once. In our case, to model the network evolution since the epoch of last scattering, we would need to follow it over a period during which the Universe expands by a factor of order 10^3 , which is not achievable, even with the current supercomputing facilities. Moreover, applying the results of the small-angle approximation would turn out to be difficult in such a case. Indeed, if z_i denotes the redshift at which we start the numerical computation, the numerical box corresponds to a real comoving size

$$L_{\text{sim}} = \frac{2/d_{h_0}}{a_0 H_0 \sqrt{\Omega_m} \sqrt{1+z_i}}, \quad (9)$$

in the matter-dominated era and for a flat universe. The density parameter Ω_m refers to the matter content of the Universe today, whereas d_{h_0} is expressed in units of the numerical box size. For the largest simulations to date, $z_i = 1089$ and $d_{h_0} \simeq 5 \times 10^{-2}$ are typical values of these two parameters (see, e.g., Ref. [28]). In a flat Λ CDM universe, using fiducial values for the density parameters compatible with the three-year Wilkinson Microwave Anisotropy Probe (WMAP) data [7], this gives $L_{\text{sim}} \simeq 9$ Gpc and the numerical box then subtends an angular size of $\theta_{\text{fov}} \simeq 27^\circ$. The largest structures in such a map would therefore be out of the small-angle limit we are interested in. As a result, we adopt the approach introduced in Ref. [33], which relies on two smaller runs. The first one starts at the last scattering surface and ends at a redshift fixed by the maximum expansion factor achievable in the numerical box. For the simulations we performed, $d_{h_0} \simeq 0.185$, which corresponds to $L_{\text{sim}} \simeq 1.7$ Gpc and $\theta_{\text{fov}} \simeq 7.2^\circ$. Such a run ends after a 30-fold increase in expansion factor, corresponding to a redshift $z \simeq 36$. We then propagate the photons perturbed by the first run into a second numerical simulation of the same size but starting at $z_i \simeq 36$. For another 30-fold increase in expansion factor, this run ends at $z \simeq 0.3$. As can be seen in Eq. (9), the second simulation represents a much larger real volume than the first one and therefore subtends a greater angle in the sky. As a result, only the subpart of the second run that matches the angle subtended by the first simulation is actually used. As we will see later on, the CMB temperature maps are weakly sensitive to the string network at low redshifts, simply because there are almost no strings intercepting our past light cone in a recent past, which makes this technique perfectly acceptable.

In practice, each of these numerical simulations is started before the redshifts we mentioned in order to give the cosmic string network enough time to relax toward its stable cosmological configuration. As soon as this scaling regime is established, the string characteristic lengths evolve in a self-similar way with respect to the horizon

size, allowing the numerical results to be rescaled to cosmological distances. Therefore, one has to make sure that the structures (strings and loops) we are interested in have indeed reached their scaling behavior during the numerical runs. This is not an issue for the so-called infinite (or long) strings, defined as strings larger than the horizon size, because they rapidly reach the scaling regime. Although it has been shown in Ref. [28] that the cosmic string loop distribution scales as well, the relaxation time for the loops to reach such a self-similar evolution with respect to the horizon size appears to be larger for smaller loops. As a result, and this is inherent to all cosmic string numerical simulations, the smaller length scales in a numerical string network keep some memory of the initial network configuration until they reach their stable cosmological evolution (see also Refs. [27, 60, 61]). Note that even if this memory effect is physical, one does not expect a physical string network at the last scattering surface to still exhibit structures coming from its initial configuration at the GUT energy scale. The change in scale factor between the GUT redshift and the last scattering surface is indeed so huge that all the observable length scales should be in scaling at decoupling. Unfortunately, as already mentioned, numerical simulations cannot probe the evolution of a cosmic string network up to the GUT epoch. To circumvent this issue, we switch on the photon propagation inside the runs only after making sure all the large structures (infinite strings and loops) are in their scaling regime. This can be checked, for instance, by monitoring the evolution of the energy density distributions. In the following, we start the photons' propagation when all loops larger than a third of the horizon size are in scaling. This cutoff is then dynamically pushed toward smaller values to include all the loops entering the scaling regime at later times. The cutoff time dependence can be deduced from the loop distribution relaxation times derived in the simulations performed in Ref. [28]. We discuss the residual systematic errors associated with the presence of nonscaling structures in Sec. II C. Finally, let us point out that our Nambu-Goto simulations are not smoothing out the so-called “small-scale structure” along the strings [22]. As a result, the CMB maps we generate depend on only one parameter, namely, the string energy per unit length U .

C. Temperature fluctuation maps

The CMB temperature fluctuations induced by strings on a 7.2° field of view are shown in Fig. 1. The upper left (respectively, right) image corresponds to the temperature fluctuations obtained at the end of the first (respectively, second) run mentioned above. The image in the top left panel exhibits more structures in the temperature patterns than the one in the top right corner. This property comes from the cosmological scaling of long strings which implies that their number inside a Hubble volume remains approximately constant during the expansion of

the Universe. As a result, since the Hubble radius grows with cosmic time, the number of long strings intercepting our past light cone on a given field of view is higher at high redshift. It turns out that most of the visible long strings end up being located close to the last scattering surface. Since this implies a small contribution from nearby strings, we did not perform a third simulation to fill the redshift gap between $z = 0.3$ and $z = 0$.

The overall CMB temperature fluctuations are plotted in the bottom left panel, while the positions of all the strings intercepting our past light cone are represented as a function of the redshift of interception in the bottom right corner. As can be seen on these images, the temperature fluctuations appear as a superposition of discontinuities associated with the long string segments. The presence of sharp edges is due to the motion of these segments with respect to the observer, which induces the typical Doppler shift associated with the Gott-Kaiser-Stebbins effect [9, 10]. Moreover, a few bright dipolar spots are visible and come from regions rich in loops and wiggly strings. These spots can be associated with the cusps appearing on some isolated loops and with the kinks sourced in the active regions of string intersections and loop formation [58]. Although the overall temperature map is dominated by the long strings pattern, the fluctuations induced by cusps and kinks may reach very high values. In fact, since the bright dipoles come from extremely localized regions, the amplitude of the temperature jump is smoothed on the scale of a pixel and increases with increasing image resolution until it reaches its physical value. As can be seen in Fig. 1, the string-induced fluctuations observed with a resolution angle of $\theta_{\text{res}} = 0.42'$ (1024 pixels) clearly exhibit highly non-Gaussian structures. The basic statistical properties of these maps are further discussed in Sec. III.

D. Robustness

The CMB temperature fluctuations maps shown in Fig. 1 have been produced using the method described in Sec. II B to minimize the influence of the numerical initial conditions. The cutoff is adjusted at each redshift to keep all the loops which have entered their expected stable cosmological evolution and remove all the smaller loops which may come from the relaxation of the initial network configuration. A side effect of this procedure is to also remove the small loops which may be produced during the stable cosmological regime. Depending on the importance of these small loops on the resulting CMB temperature fluctuations, the simulated maps we obtain may therefore deviate from the ones that would be induced by a real string network. In order to quantify this deviation, we can compare our results (i.e., the map shown in the bottom left corner of Fig. 1, thereafter, the “reference map”) to the maps computed in two extreme cases: when all the loops are removed from the runs, and when all the loops, even the smallest ones believed

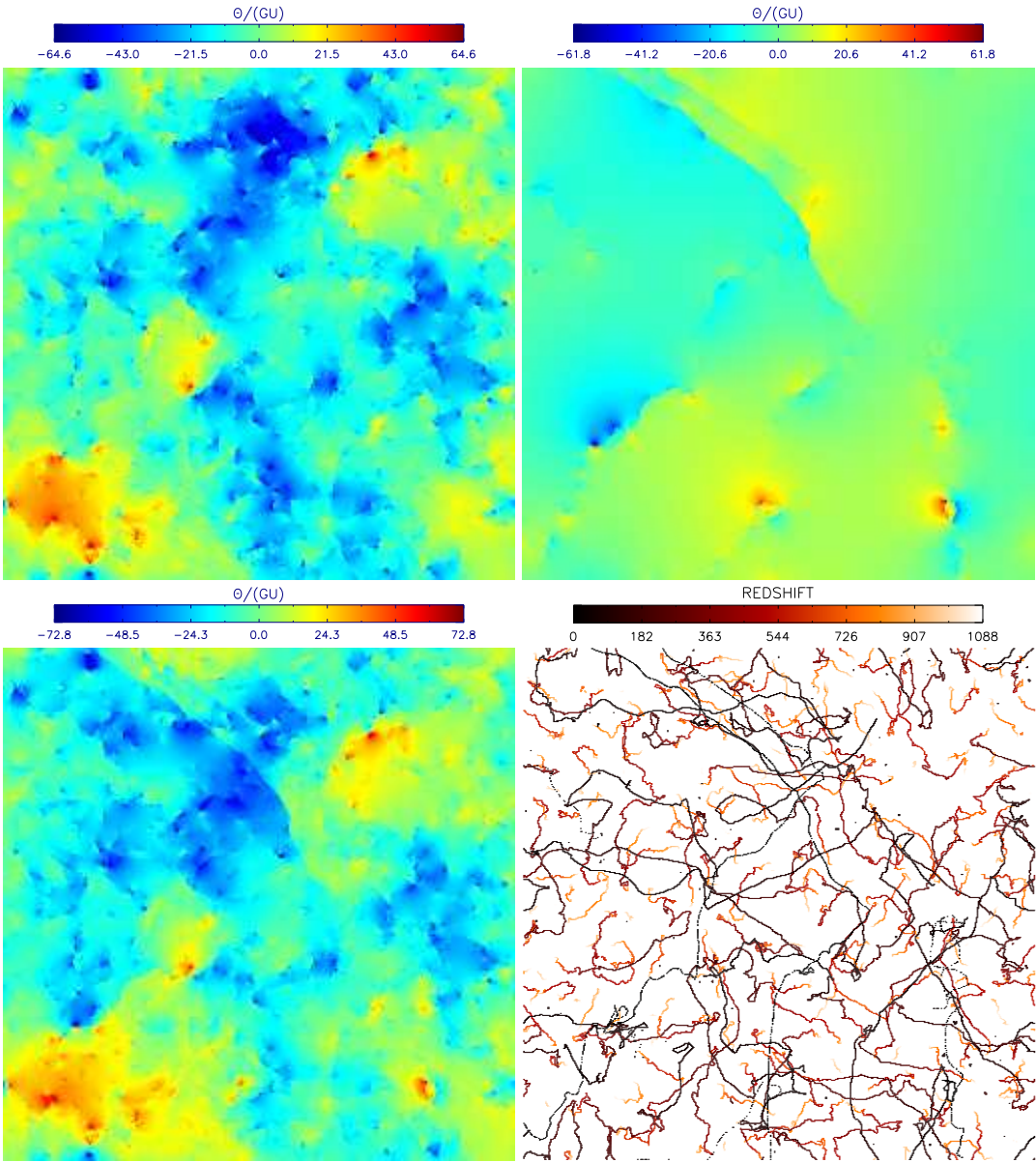


FIG. 1: String-induced CMB temperature fluctuations on a 7.2° field with a (unrealistic) resolution of $\theta_{\text{res}} = 0.42'$ (1024 pixels). The upper left image shows the fluctuations induced in between the last scattering surface and the redshift $z = 36$, while the upper right map represents the anisotropies produced by strings between $z = 36$ and $z = 0.3$. Because of their cosmological scaling, most of the long strings intercept our past light cone close to the last scattering surface. The overall string-induced fluctuations are plotted in the bottom left panel. As can be seen in the bottom right image, the edges in the temperature patterns of the other maps can be identified to strings intercepting our past light cone. Note that active regions corresponding to string intersection and loop formation events lead to the bright spots in these maps. Some of these spots are associated with $\Theta > 80 \text{ GU}$ and saturate the color scale (see Sec. III).

to come from the initial conditions, are kept. Those results are shown in Fig. 2. As one may expect, the deviations are most apparent on the smallest scales. When all loops are included, the altered map differs from the reference map by about 10%. The difference is a primarily small-scale noise with a few bright dipolar spots coming from the tiny loops. The situation is similar for the map obtained by removing all the loops. In that case, the

few dipoles and large-scale structures produced by the loops in scaling are missing. Thanks to these “extreme” maps, we are now able to estimate the systematic errors associated with the presence of nonscaling structure in our numerical simulations. This is in particular useful to see how robust are the basic statistical properties of our maps, which we discuss in Sec. III.

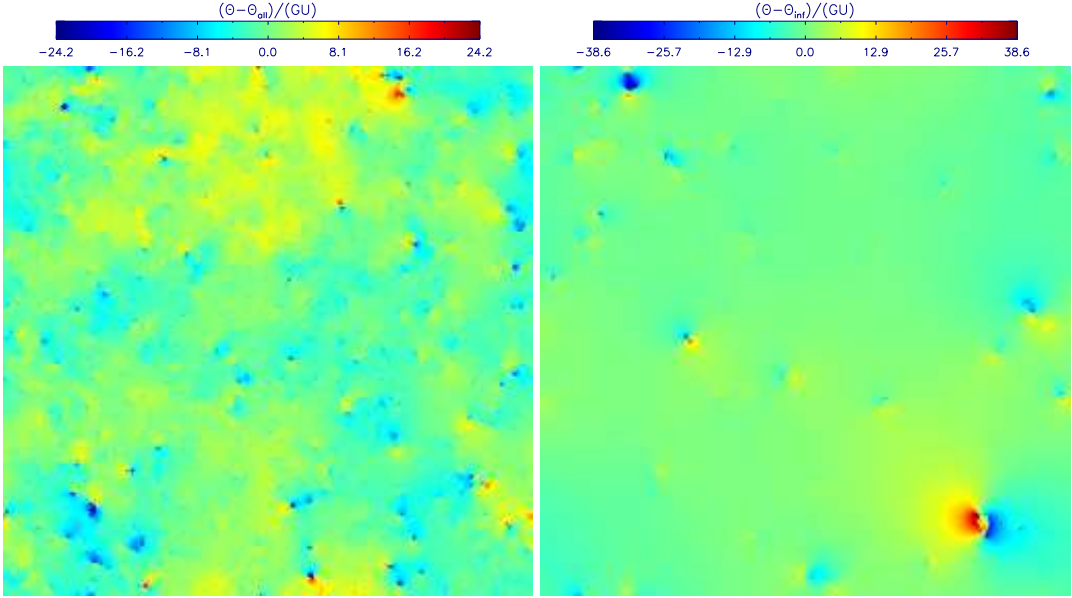


FIG. 2: Influence of the nonscaling structures on the computed CMB temperature maps. Θ_{all} (respectively, Θ_{inf}) refers to the CMB fluctuations that would be obtained by keeping (respectively, removing) all loops present in the numerical simulations, including the spurious ones coming from the relaxation of the numerical initial conditions. The left (respectively, right) panel shows the deviation induced by the presence (respectively, absence) of these structures with respect to the reference temperature map shown in the bottom left corner of Fig. 1. We use these maps in Sec. III to estimate the systematic errors induced by the presence of nonscaling structures in the cosmic string simulations.

III. BASIC STATISTICAL PROPERTIES

The CMB temperature patterns are directly related to the properties of the strings intercepting our past light cone in a particular realization of the associated network (see Fig. 1). In order to extract meaningful properties from the string-induced CMB anisotropies, we generate 84 statistically independent maps following the techniques described in Sec. II. Two CPU years have been devoted to performing 28 runs starting from statistically independent Vachaspati-Vilenkin initial conditions (on IBM Power4 P660+ and AMD x86-64 2 GHz processors). Each of these numerical simulations gives three temperature maps along the three spatial directions that can be used as either the low or high redshift contribution. Finally, the overall temperature anisotropies map is obtained by combining a low and a high redshift map coming from two different runs.

A. One-point distribution function

The non-Gaussian nature of the temperature fluctuations induced by strings produces a very characteristic pattern on the maps shown in Fig. 1. A simple quantitative test of this feature is given by the one-point probability distribution function (PDF) of the temperature anisotropies. The normalized PDF has been derived in three cases: temperature anisotropies generated by the

infinite strings only (Θ_{inf} map), by the strings and loops in scaling, and by all the structures (Θ_{all} map). The corresponding PDF's averaged over all the simulated maps are shown in the left panel of Fig. 3. In each case, the PDF unambiguously deviates from a Gaussian as can be seen by comparison to the best Gaussian fit to our best PDF estimate (corresponding to the case where only strings and loops in scaling are taken into account). It is also worth pointing out that the result is relatively insensitive to the inclusion of loops, although including non-scaling structures increases the width of the distribution.

More quantitatively, the mean of the distribution is zero to better than one part in 10^5 , whereas the variance averaged over all 84 maps is $\langle \sigma_s^2 \rangle \simeq 154_{-8}^{+24} (GU)^2 T_{\text{CMB}}^2$. The systematic errors quoted in this result have been derived from the mean values of the variance coming from the Θ_{all} (upper bound) and Θ_{inf} (lower bound) maps. A power-law fit of the tails of the PDF's restricted to fluctuations with $|\Theta| > 50 GU$ shows that they vary as Θ^{-q} with $q = 8.2 \pm 0.2$, which, although steep, decays much more slowly than a Gaussian.

As can be seen in the shape of the PDF compared to the best Gaussian fit, we have also measured a slight negative mean sample skewness

$$\langle g_1 \rangle \equiv \left\langle \frac{(\bar{\Theta} - \Theta)^3}{\sigma^3} \right\rangle \simeq -0.24, \quad (10)$$

where $\langle \cdot \rangle$ again refers to the average over all 84 maps, whereas a bar corresponds to an average over a single

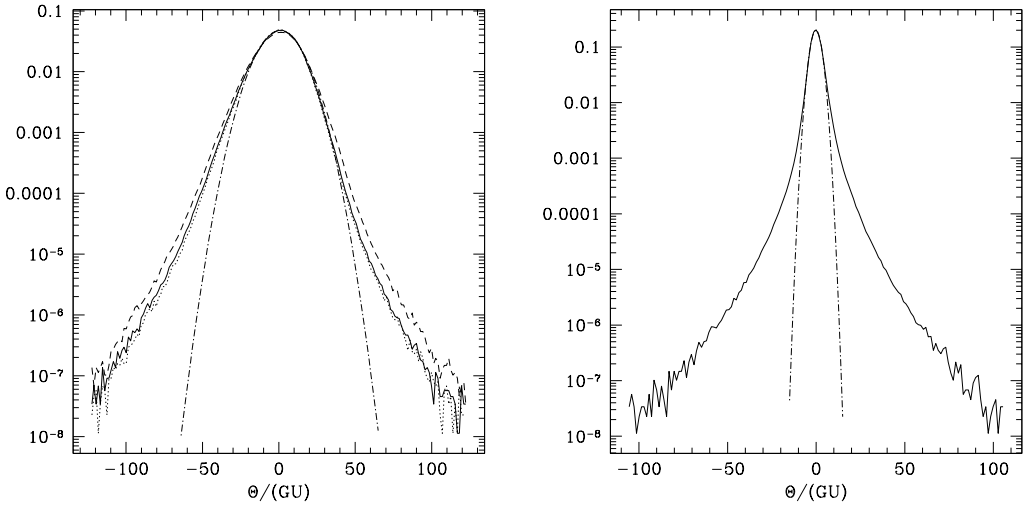


FIG. 3: The left panel shows the probability distribution function of the CMB temperature fluctuations induced by cosmic strings (solid line). The dotted and dashed curves quantify the systematic errors coming from the string simulations. Each of these one-point functions is averaged over 84 independent realizations. The dash-dotted curve represents the best Gaussian fit. Deviations from Gaussianity are clearly apparent in the tails of the distribution, as well as from the slight skewness. The right panel shows the probability distribution function of the CMB temperature fluctuations that would have been induced by the nonscaling structures, as defined in Sec. II D. Once again, the dash-dotted curve represents the best Gaussian fit. A slight positive skewness may be observed, suggesting that the negative skewness observed in the left panel is the result of the loop formation mechanism.

map. Although the dispersion of g_1 between the maps is significant, there is a clear preference for $g_1 < 0$ with less than 15% of our maps exhibiting a positive skewness. This skewness may come from high correlations between the string velocities and the shape of the strings along the past light cone. To confirm this, we checked that the skewness disappears if the velocity field along the long strings is randomly redistributed. Since the shape and velocity field of strings strongly depend on their nonlinear evolution, which itself relies on intercommutation and loops formation, one may interpret this effect as a consequence of their nontrivial interactions. This interpretation can be further explored by looking at the PDF of the temperature fluctuations associated with the “non-scaling” structures, as defined in Sec. II D. This PDF is shown in the right panel of Fig. 3 and exhibits a slightly positive skewness. Two kinds of structures contribute to this PDF: the tiny loops generated during the stable cosmological evolution of the network, and the loops generated by relaxation of the initial conditions. It is precisely because of the difficulty of distinguishing the physical loops from the ones associated with the relaxation of the initial conditions that we discarded these structures when generating our maps. As a result, we stress that using this PDF as a tool to understand the physics is not straightforward. The fact that the PDF shown in the right panel of Fig. 3 is also skewed supports the existence of the correlations mentioned above. However, since the nonscaling structures are by definition still sensitive to the numerical initial conditions, the bare

value of the skewness given in Eq. (10) should be taken with a grain of salt. In particular, one may not exclude a smaller value if all the loops were evolving in their scaling regime, as it should be for a physical string network. To complement this qualitative explanation, it would be interesting to try to understand this effect quantitatively using analytical methods, such as the velocity dependent one-scale model of Refs. [62, 63]. Let us finish this discussion by pointing out that the value of the kurtosis for the PDF presented in the left panel of Fig. 3 is

$$\langle g_2 \rangle \equiv \left\langle \frac{(\Theta - \bar{\Theta})^4}{\sigma^4} \right\rangle - 3 \simeq 0.63. \quad (11)$$

Gaussian fluctuations, such as the primary anisotropies of inflationary origin, are entirely described by their one-point distribution and two-point correlation functions. As the string-induced anisotropies are not Gaussian, the angular power spectrum does not contain all the statistical information associated with them, but provides a way of estimating their relative contribution to the CMB anisotropies as a function of angular scale.

B. Power spectrum

The two-dimensional power spectrum of the string-induced temperature anisotropies can easily be derived

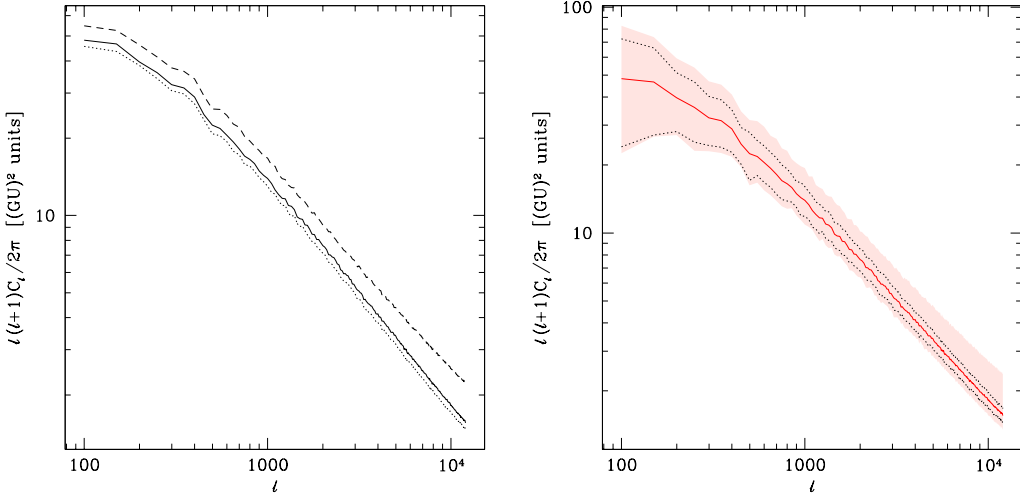


FIG. 4: Mean (over our 84 maps) of the angular power spectrum of string-induced CMB anisotropies (solid lines). In the left panel, the dashed (respectively, dotted) line is the mean power spectrum obtained from string simulations including all loops (respectively, infinite strings only). These two curves give an estimate of the systematic error in the results derived from our numerical simulations. In the right panel, the dotted lines define the $\pm 1\sigma$ statistical error envelope around our best estimate of the power spectrum. The shaded area includes the effect of our systematic errors in addition to the statistical ones.

in Fourier space. Assuming statistical isotropy,

$$P(u) = \left| \frac{1}{GU} \int \Theta(\alpha, \beta) e^{-i\mathbf{u}\cdot\theta} d^2\theta \right|^2, \quad (12)$$

where $\theta \equiv (\alpha, \beta)$ denotes angular coordinates and \mathbf{u} the two-dimensional wave vector. In the small-angle approximation, this is also the angular power spectrum up to a redefinition of the wave number [64]. We have

$$\frac{\ell(\ell+1)}{4\pi^2} C_\ell \simeq u^2 P(u), \quad (13)$$

with $u = \ell/(2\pi)$, which we use to produce Fig. 4. For a field of view of 7.2° and a resolution of $0.42'$, the multipole moments run from $\ell \simeq 10^2$ to 10^4 . As detailed in Sec. II, we only take the string-induced ISW effect into account when computing the CMB temperature fluctuations from strings. As a result, the spectra we present in this section are only accurate at small angular scales, typically for multipoles higher than a few hundred. The left panel of Fig. 4 shows three spectra averaged over our 84 maps. The central one corresponds to our best estimate, whereas the top and bottom spectra have been, respectively, obtained from the string-induced temperature anisotropies Θ_{all} and Θ_{inf} and trace the systematic error in the power spectrum estimation (see Sec. II D). In the right panel, we show our best estimate of the power spectrum, as well as of the associated systematic and statistical errors combined. We define this combination as the smallest area around our best estimate containing all the $\pm 1\sigma$ statistical error envelopes of the spectra presented in the left panel.

Although the uncertainties induced by the presence of nonscaling structures in the simulations affect the overall normalization of the spectrum, its global shape remains the same. Using a power law fit to the small-angle tail of the spectrum,

$$\ell(\ell+1) C_\ell \underset{\ell \gg 1}{\propto} \ell^{-p} \quad \text{with} \quad p = 0.889^{+0.001}_{-0.090}, \quad (14)$$

where we only quote systematic errors estimated from the extreme power spectra shown in the left panel of Fig. 4. Let us point out the fact that the overall amplitude, in units of GU , of our best estimate spectrum appears to be compatible with the one recently obtained for Abelian strings at large angular scales by the UTC method [19]. At multipole $\ell = 1000$, we have $\ell(\ell+1) C_\ell/(2\pi) \simeq 14(GU)^2$. It is nice to see these two techniques agree over the range of multipoles where they are both valid approximations, but it is not trivial that this should be the case. In particular, numerical simulations of Abelian string networks do not exhibit the typical loop formation events observed for Nambu-Goto strings [24, 25]. However, the scaling regime of long strings is reached in both Abelian and Nambu-Goto simulations. As already discussed, the typical distance between long strings in scaling at the surface of last scattering is a fraction, typically a fifth [28], of the Hubble radius at that time. As a result, even the long strings are contributing to the CMB anisotropies down to moderately small angles. It is therefore not totally surprising that both spectra are similar at intermediate angular scales ($1000 \lesssim \ell \lesssim 3000$). We do not try to compare our results to those presented in [19] at larger angular scales since our method relies on the flat-sky approxima-

tion, which breaks down for multipoles smaller than a few hundred.

As can be seen in Fig. 4, some extra power shows up at very small scales for the C_ℓ 's coming from the numerical simulations including the nonscaling loops (Θ_{all}). The same effect was already visible on the corresponding temperature map plotted in Fig. 2 (left panel) and suggests that nonscaling structures start to have significant effects at very small scales, for $\ell \gtrsim 10^4$. The very small-scale effect of loops (be they in scaling or not) is also what explains the asymmetric errors appearing in Eq. (14). As expected from the presence of cosmic strings all along our past light cone, the power spectrum decays quite slowly at small angular scales, and much slower than the exponential Silk damping experienced by the CMB anisotropies of inflationary origin. As a result, a contribution of cosmic strings to the angular power spectrum could be negligible at low multipoles and yet dominate the primary anisotropies for large values of ℓ . We discuss the observability of string-induced anisotropies at small scales in more detail in Sec. IV.

C. Gradient magnitude as a string tracer

Although the one- and two-point functions already exhibit some characteristic features of string-induced CMB anisotropies, they remain weakly sensitive to most of the highly non-Gaussian features one can see in Fig. 1. More sophisticated statistical tools have been developed to look for patterns in the CMB. These techniques involve the use of Minkowski functionals, the skeleton, wavelet analysis, or temperature step finders, among others [29, 65, 66, 67, 68]. The corresponding estimators are usually applied directly on CMB temperature maps. However, the deviations from Gaussianity appearing in the PDF shown in the left panel of Fig. 3 are due to two main effects, namely, the presence of rare high temperature events coming from localized string and loop regions with kinks and cusps, and the linelike (and fractal) shape of the temperature steps induced by moving strings in the microwave sky, which also explains the power-law behavior of the power spectrum at small angular scales. One may therefore expect such estimators to be more efficient when directly applied to a string map, such as the one shown in the bottom right panel of Fig. 1. Of course, such a map cannot be directly observed. But since strings appear as discontinuities in the temperature maps, the temperature gradient would be singular at the string location, enabling us to produce a map similar to the one shown in the bottom right panel of Fig. 1, though with no redshift information. This map could then be used with the techniques mentioned above to get more statistical information on the properties of networks of strings.

Directional gradients were first discussed in Ref. [69] to analyze the topology of string-induced temperature anisotropies. In order to conserve isotropy, it is convenient to consider the gradient magnitude $|\nabla\Theta|$ of the

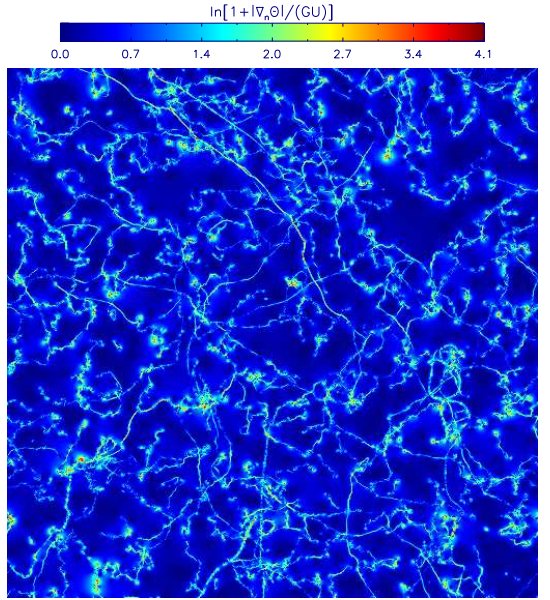


FIG. 5: Normalized gradient magnitude of the string-induced temperature anisotropies shown in Fig. 1 (bottom left panel). A logarithmic scale has been used to enhance the contrast by preventing the bright spots from saturating the color scale. Such a map reproduces the string path on our past light cone and enhances the active string regions (see Fig. 1).

temperature anisotropies defined by

$$|\nabla\Theta| \equiv \sqrt{\left(\frac{d\Theta}{d\alpha}\right)^2 + \left(\frac{d\Theta}{d\beta}\right)^2}, \quad (15)$$

where α and β are the horizontal and vertical angular coordinates. This definition makes it clear that for a finite temperature step, let us say $\Theta(\alpha, \beta) = \Theta_0 H(\alpha - \alpha_0)$, H being the Heaviside function, the resulting gradient magnitude is a Dirac distribution at the string location. On a pixelized map, the maximal amplitude of $|\nabla\Theta|$ is therefore given by the size of each pixel. To take this resolution effect into account, we instead look at the normalized gradient magnitude $|\nabla_n\Theta|/GU$, defined by

$$|\nabla_n\Theta| \equiv |\nabla\Theta| \theta_{\text{res}}, \quad (16)$$

of the temperature map shown in the bottom left panel of Fig. 1. The resulting map is shown in Fig. 5. Note that we enhanced the contrast by using a logarithmic scale to prevent the bright dipoles from saturating the color scale. As can be checked by comparing Fig. 5 to the bottom right panel of Fig. 1, the gradient map reproduces the string path on our past light cone. In addition, the magnitude of the gradient, once normalized to the image resolution, encodes the transverse string velocity, which renders kinks and cusps clearly visible. But since all the results presented in this section have been derived for strings alone, and with a high and quite unrealistic angular resolution, one may question their relevance in

view of the current experiments and data. In the next section, we address this issue by combining the string-induced anisotropies with the standard primary and expected secondary CMB signals for a typical arcminute-resolution CMB experiment.

IV. OBSERVING COSMIC STRINGS

CMB experiments have so far been able to map the microwave sky down to scales corresponding to multipoles of order 2×10^3 , WMAP providing cosmic variance limited measurements up to $\ell \sim 400$ [7]. At these scales, the primary CMB dominates over all secondary effects by more than an order of magnitude. However, upcoming experiments will produce CMB maps with arcminute resolution, at which point secondary effects become the dominant source of fluctuations [30, 31, 32]. It is therefore crucial to take them into account to produce reasonably realistic maps of what the CMB would look like at small angular scales in the presence of strings. Throughout this section, we consider a flat power-law Λ CDM cosmology with $h = 0.70$, $\Omega_\Lambda = 0.73$, $\Omega_b = 0.045$, $n_s = 0.95$, $\Omega_m = 0.27$, $\sigma_8 = 0.78$ and $\tau = 0.073$. The hydrogen fraction is set to 0.76.

A. Contribution of secondary anisotropies

In the flat-sky limit, provided that the angular scale be small enough for the two-halo term to be negligible, the thermal Sunyaev-Zel'dovich effect (tSZ) angular power spectrum can be computed in the context of the halo formalism and is then given by [70, 71, 72]

$$C_\ell = \left(x \frac{e^x + 1}{e^x - 1} - 4 \right)^2 \int_0^{z_{\max}} dz \frac{dV(z)}{dz} \times \int_{M_{\min}}^{M_{\max}} dM \frac{dn(M, z)}{dM} |\tilde{y}_\ell(M, z)|^2, \quad (17)$$

where $x = h\nu/k_B T_{\text{CMB}}$, $V(z)$ is the comoving volume at redshift z per steradian, dn/dM is the comoving number density of dark matter halos of mass M at redshift z , and $\tilde{y}_\ell(M, z)$ is the Fourier transform of the projected Compton y parameter. To compute $dn(M, z)/dM$, we use the Jenkins mass function [73], and the linear matter power spectrum produced by **CAMB** [74]. $\tilde{y}_\ell(M, z)$ is calculated as in Ref. [72], the tSZ profile being integrated over a maximum of two virial radii. At the angular scales of interest, the values of z_{\max} , M_{\min} , and M_{\max} have been set according to Ref. [72] and are accurate enough to ensure the convergence of the integrals. However, there are several theoretical uncertainties in the calculation of the mass function and the Compton y parameter, leading to a typical uncertainty of a factor of 2 on the overall amplitude of the tSZ spectrum. Moreover, as the two-halo term is neglected, the current approach holds only for $\ell > \ell_{\max} \simeq 300$ [75]. This limitation is unimportant for

our study as the primary CMB dominates over all other secondary effects by more than 3 orders of magnitude for multipoles smaller than ℓ_{\max} .

The kinetic Sunyaev-Zel'dovich effect (kSZ) has been computed exactly in the linear regime, where it is also known as the Ostriker-Vishniac (OV) effect [76, 77, 78]. Although no exact result exists in the nonlinear regime, several analytical models have been proposed to describe this component [79, 80, 81]. Here, we use the model of Ref. [81] with, as input, the same linear matter power spectrum generated by **CAMB** as for the tSZ. Although the nonlinear corrections are unimportant at large scales, they become significant in the small-angle limit. Within our cosmological model, assuming instantaneous reionization, the nonlinear component of the kSZ has the same amplitude as the linear one at $\ell \sim 2500$.

Several other secondary effects can produce fluctuations in the CMB temperature, among which are gravitational lensing, the ISW and Rees-Sciama effects linked to the standard cosmological fluids, patchy reionization, and point sources. The corrections to the primary anisotropies due to gravitational lensing have been included and computed with **CAMB**. Though they become important relative to the primary anisotropies for $\ell \geq 2000$, the Sunyaev-Zel'dovich effects are always dominant at these scales. The ISW and Rees-Sciama effects linked to the standard cosmological fluids are never dominant secondary effects for $\ell \geq 100$ [82], and we therefore ignore them. It has been shown that patchy reionization can make a significant contribution to the nonlinear kSZ, though an agreement on how big this contribution is is still to be found [83, 84, 85]. Given the uncertainties involved in this effect and the fact that, even if the signal coming from patchy reionization dominates the nonlinear kSZ, it is still at least an order of magnitude smaller than the tSZ at all scales [85], we do not include it in our analysis. Finally, the question of how one should deal with point sources is probably the trickiest one. Modeling point sources (be they radio or infrared ones) is indeed an arduous task leading to quite uncertain models [86], which leads us to omit them in the present analysis. This is a clear limitation of our study that should be kept in mind when trying to use the results presented here to predict how well we could be able to do as far as detecting cosmic strings is concerned. Although complementary observations at other wavelengths will help in removing the signal from the brightest point sources [32], our ability to remove the remaining contamination will limit the possibility of detecting the signature of cosmic strings in the microwave sky. This should be yet another motivation for trying to improve our understanding of point sources and develop efficient techniques to remove them without losing interesting string-induced features.

The angular power spectra of all these effects, namely, lensed primary anisotropies, tSZ, OV, and nonlinear kSZ, are shown in the left panel of Fig. 6, along with various spectra of the anisotropies induced by cosmic strings. From top to bottom, the string power spectra have been

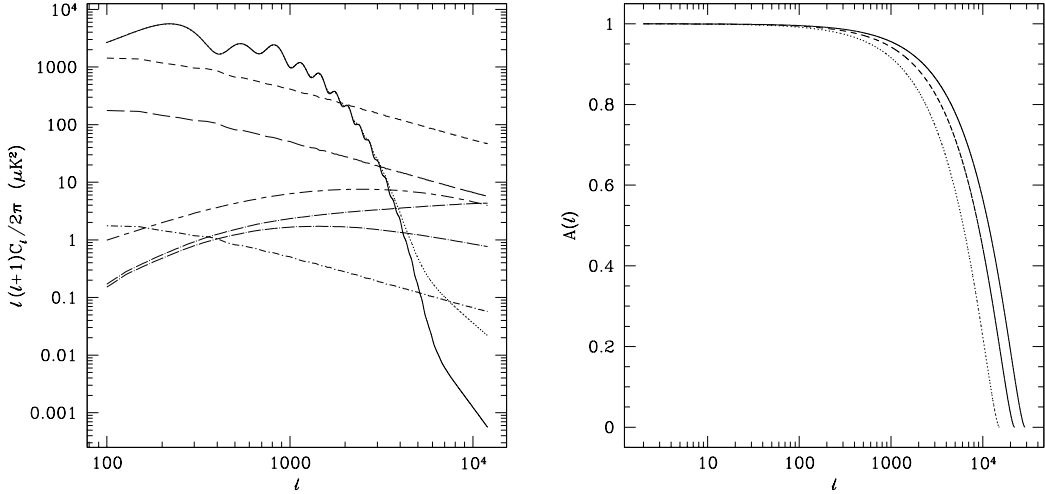


FIG. 6: (Left) Angular power spectrum of the primary CMB anisotropies (solid line), the lensed CMB (dotted line), the thermal Sunyaev-Zel'dovich effect (long dashed-short dashed line), the Ostriker-Vishniac effect (lower long dash-dotted line), and the nonlinear kinetic Sunyaev-Zel'dovich effect (upper long dash-dotted line) in a flat power-law Λ CDM universe (see text). The fluctuations generated by cosmic strings are shown for three values of the string tension: $GU = 2 \times 10^{-6}$ (short dashed line), 7×10^{-7} (long dashed line), and 7×10^{-8} (short dash-dotted line). (Right) Model of the primary ACT beam in multipole space at 279 GHz (solid line), 215 GHz (dashed line) and 147 GHz (dotted line). The normalization is chosen such that the beam is unity at $\ell = 0$. As expected for a diffraction-limited beam, the cutoff multipole increases with increasing frequency.

generated with $GU = 2 \times 10^{-6}$, 7×10^{-7} , and 7×10^{-8} . The tension 2×10^{-6} is the one required to normalize the large-scale string-induced power spectrum presented in Ref. [19] to the WMAP three-year data at $\ell = 10$. Such a high value of the string tension is already ruled out at more than 3σ [87], but is commonly used as a reference. $GU = 7 \times 10^{-7}$ is the 95% confidence level upper limit set in Ref. [88] with the power spectrum presented in Ref. [19]. Since the amplitude of our string spectrum at $\ell \simeq 1000$ matches the one derived in this reference (see Sec. IIIB), we use $GU = 7 \times 10^{-7}$ to produce the maps shown in Figs. 8 and 9. Let us point out the fact that the associated string spectrum becomes marginally dominant over all primary and secondary anisotropies for multipoles larger than typically 3×10^3 . However, for smaller tensions, the dependence of the amplitude of the string-induced power spectrum on $(GU)^2$ rapidly brings the latter below the spectra of all the secondary anisotropies we consider for ℓ above a few hundred. This is the case, e.g., for $GU = 7 \times 10^{-8}$. Because of this strong dependence on GU , the factor of 2 uncertainty on the amplitude of the tSZ is relatively unimportant for our study.

Combining all these results, we can now generate simulated maps of the temperature fluctuations produced by the corresponding primary and secondary effects and add them to the string-induced anisotropies. However, to more realistically predict what arcminute-resolution CMB observations would look like in the presence of strings, we also need to convolve the resulting maps with a model for the beam of such an experiment.

B. Instrument beam

Several arcminute-resolution CMB experiments are already underway, covering frequencies from 15 GHz [30] all the way to 345 GHz [31]. In the remaining of this paper, we will use a model based on the ACT specifications to include realistic resolution effects in our maps. ACT is a 6 m telescope that will map the microwave sky at 147, 215, and 279 GHz [32]. The actual data collected in such an experiment is not directly the temperature on the sky, but the result \mathcal{V} of the convolution of the latter with the instrument beam such that [64]

$$\mathcal{V}(\mathbf{k}) = \frac{\partial B_\nu(T)}{\partial T} T_{\text{CMB}} \int \Theta(\mathbf{r}) A(\mathbf{r}) e^{-i\mathbf{k}\cdot\mathbf{r}} d^2\mathbf{r}, \quad (18)$$

where $B_\nu(T)$ is the Planck function, \mathbf{r} the coordinates of a point on the telescope, and $A(\mathbf{r})$ the primary beam that we model as an Airy pattern. We are interested in the Fourier transform of the primary beam per unit area,

$$\tilde{A}(u) = \mathcal{A} \left[\arccos \frac{u}{u_c} - \frac{u}{u_c} \sqrt{1 - \left(\frac{u}{u_c} \right)^2} \right], \quad (19)$$

where $u \equiv k/(2\pi)$, $\mathcal{A} \equiv 2/(\pi^4 d^2)$, and $d = 6$ m. The beam in Eq. (19) is defined for $u < u_c$, where, at a given wavelength λ , $u_c = \theta/\lambda$, with θ the characteristic maximum opening of the telescope set to 70° [89]. For $u > u_c$, $\tilde{A}(u) = 0$. The normalization is chosen such that, with

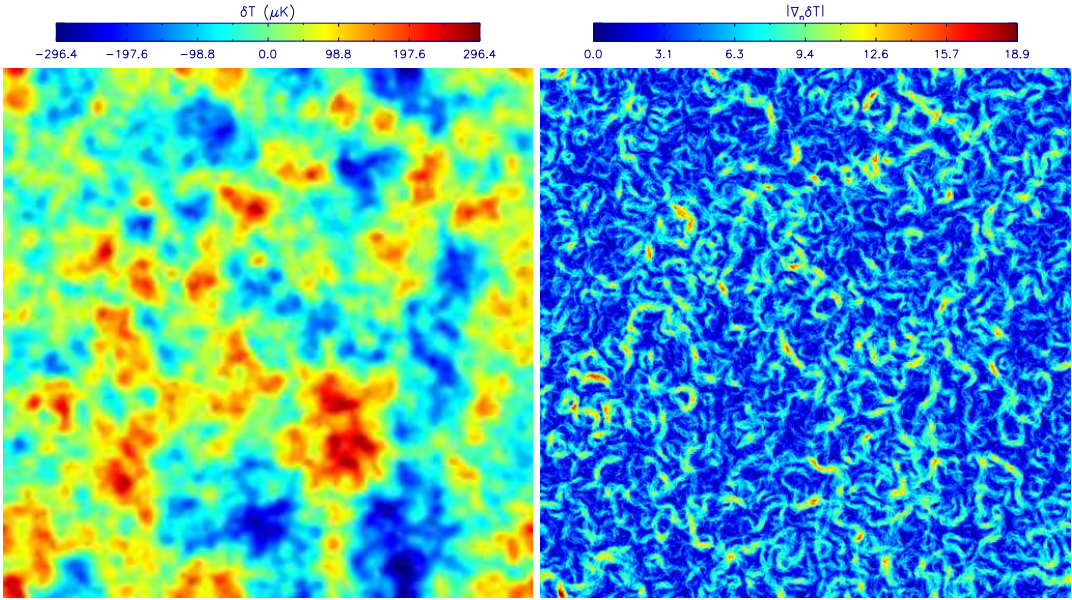


FIG. 7: CMB temperature anisotropies, including the lensed primary fluctuations predicted by our fiducial Λ CDM model (see text), as well as the tSZ, OV, and nonlinear kSZ effects, for a 7.2° field of view at 147 GHz (left), and corresponding normalized temperature gradient magnitude map (right). These maps take into account the effect of the primary ACT beam as derived in Sec. IV B. The effect of strings is *not* included.

the convention

$$A(\mathbf{r}) = \frac{1}{(2\pi)^2} \int \tilde{A}(\mathbf{u}) e^{2i\pi(\mathbf{u} \cdot \mathbf{r})} d^2\mathbf{u}, \quad (20)$$

$A(0) = 1$. In the small-angle approximation, Eq. (19) becomes, in multipole space,

$$\tilde{A}(\ell) = \mathcal{A} \left[\arccos \frac{\ell}{\ell_c} - \frac{\ell}{\ell_c} \sqrt{1 - \left(\frac{\ell}{\ell_c} \right)^2} \right], \quad (21)$$

with $\ell_c = 2\pi d/(\lambda\theta)$. The normalized primary beam $A(\ell) \equiv \tilde{A}(\ell)/\tilde{A}(0)$ is shown in the right panel of Fig. 6 for the three ACT frequency bands.

C. Generating mixed maps

In this section, we present small-angle maps of the CMB temperature anisotropies induced by all of the effects mentioned above. Producing these maps turns out to be relatively straightforward for two reasons: the primary anisotropies of inflationary origin, but also the secondary ones, namely, the tSZ and kSZ contributions, can be treated as Gaussian effects, and these fluctuations are uncorrelated with the string-induced anisotropies. The first of these two properties allows us to easily generate maps of the corresponding effects. Rocha *et al.* indeed showed in Ref. [90] that, assuming statistical isotropy, these maps can be produced by convolving a normalized Gaussian white noise with the power spectrum of interest. The fact that we do not need to know anything else

than the power spectrum of these effects should not be a surprise as the two-point correlation function encodes all the statistical information of Gaussian effects. Applying this technique with the spectra shown in the left panel of Fig. 6, we can therefore generate maps including the effects of all primary and secondary anisotropies. Now that we have these maps, we can use the second property mentioned above to include the effect of a network of cosmic strings. As the latter is uncorrelated with the primary and other secondary anisotropies, we indeed only have to add those maps to a map of the string-induced CMB anisotropies. The only unknown parameter controlling the overall amplitude of the string-induced temperature fluctuations is the string tension, for which we use $GU = 7 \times 10^{-7}$ (see Sec. III B). We are then left with convolving the resulting map with the primary beam calculated in Sec. IV B. While the tSZ will produce non-Gaussian spots, we can ignore them in this initial study. In practice, these sources can indeed easily be masked out of CMB maps when they correspond to bright (typically, 5σ) sources. Moreover, in the case of multi-frequency experiments, it is possible to separate thermal SZ effects from thermal CMB distortions.

We apply all these techniques to produce maps including the primary and all secondary anisotropies discussed above, as well as the effect of a network of cosmic strings. Figure 7 is given as a reference: it does not include any stringy effect. Therefore, the patterns associated with the acoustic peaks are clearly visible, as well as the Gaussian nature of the fluctuations. The right panel shows the corresponding normalized gradient magnitude, as defined

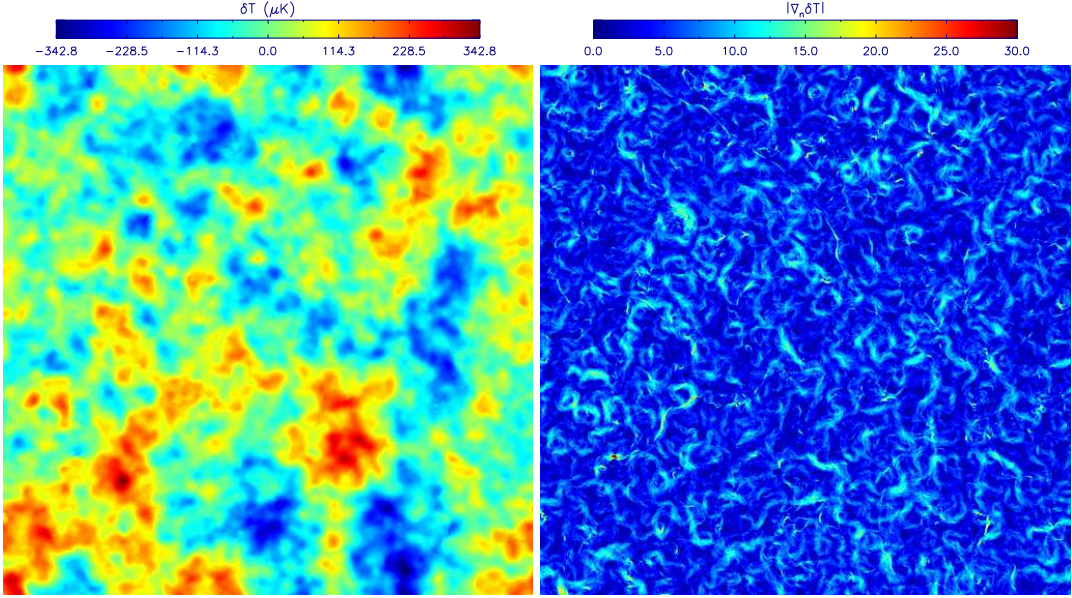


FIG. 8: CMB temperature anisotropies, including the same primary and secondary effects as in Fig. 7, as well as a string contribution of $GU = 7 \times 10^{-7}$, for a 7.2° field of view at 147 GHz (left), and corresponding normalized temperature gradient magnitude map (right). Although the presence of strings can only be guessed in the left panel, very distinctive string features appear in the right one. In addition to sharp temperature steps scattered throughout the map, a few bright dipoles can be seen in localized string and loop regions with kinks and cusps. Once again, these maps take into account the effect of the primary ACT beam as derived in Sec. IV B.

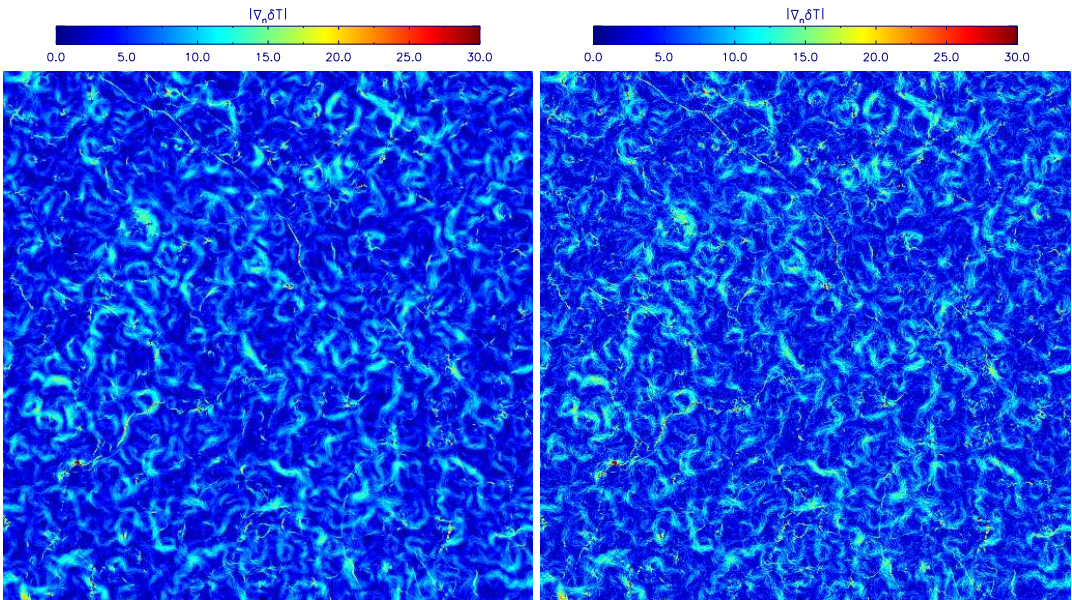


FIG. 9: Normalized temperature gradient magnitude maps with the same components as in Fig. 8, but at 215 GHz (left) and 279 GHz (right). The thermal Sunyaev-Zel'dovich effect vanishes at 215 GHz [see Eq. (17)]. The enhancement of the string signatures with increasing frequency is clearly visible when comparing this figure to the right panel of Fig. 8. Moreover, when the latter is compared to the right panel of this figure, filaments produced by the tSZ become visible at 279 GHz.

in Eqs. (15) and (16), with $\theta_{\text{res}} = 0.42'$. By construction, the resulting map is highly non-Gaussian and enhances the rapid angular variations of the temperature patches of the fluctuation map. However, these structures remain relatively smooth and, unlike the string patterns of Fig. 5, do not exhibit any saturating bright spot. As a result, we were here able to use a linear color scale.

In Fig. 8, we now include the effect of a network of strings with $GU = 7 \times 10^{-7}$. The temperature fluctuations remain dominated by the Gaussian ΛCDM signal and the secondary anisotropies, with hints of temperature steps induced by strings. Note the bright dipole in the bottom left corner of these maps: it is no longer symmetric in temperature due to the presence of the Gaussian sources. Even in the presence of the dominant primordial and secondary fluctuations, the gradient map still reveals the strings' location and velocity. However, the slow-moving segments are now hidden in the gradient of the Gaussian patterns. As a result, the “faint” strings appear to be discontinuous. The normalized gradient color scale, although linear, has been limited to 30, while some of the saturating gradient values go up to 46, as one may have expected from the PDF shown in the left panel of Fig. 3. Finally, Fig. 9 shows the gradient magnitude of the temperature fluctuations generated by the same sources at 215 GHz (left panel) and 279 GHz (right panel), whereas the maps shown in Figs. 7 and 8 assume a frequency of 147 GHz. The temperature map is not represented since it is basically identical to the one of Fig. 8. The gradient color scale is kept the same as in this figure to make the comparison with the latter easier. As can be seen on these plots, the string “brightness” increases with increasing frequency, therefore reflecting the beam frequency dependence shown in the right panel of Fig. 6. As already mentioned, the increase in angular resolution accompanying the increase in frequency enhances the gradient magnitude, but, interestingly, only for the intrinsically discontinuous anisotropies, such as the ones generated by strings. At these frequencies, the highest normalized gradient magnitudes observed go up to 65 at 215 GHz and 95 for the 279 GHz channel. As can be seen by comparing the right panel of Fig. 8 to the left panel of Fig. 9, increasing the angular resolution also induces a higher sensitivity to the secondary sources. SZ features clearly appear on the 279 GHz gradient map as small filaments, whereas they are absent on the 147 GHz map, because of the extra smoothing coming from a narrower beam. The maps shown in this section therefore suggest that upcoming arcminute-resolution CMB experiments, such as ACT, could significantly improve the current constraints on the string tension GU . In a subsequent paper, we will explore developing optimal non-Gaussian estimators aimed at detecting the coherent linelike string features in temperature and gradient maps. However, they are different enough from the features produced by the tSZ effect and other known sources of non-Gaussianity that we can already use a very naive statistic to get a crude estimate of the detection threshold that the afore-

mentioned experiments could reach. Requiring that at least of order ten linelike features be visible in our gradient maps, we can clearly see non-Gaussianities down to $GU \simeq 2 \times 10^{-7}$. We suspect that more detailed studies will yield a firmer detection limit.

V. CONCLUSION

Based on numerical simulations of Nambu-Goto cosmic string networks, we produced 84 high-resolution string-induced CMB temperature maps over a 7.2° field. We extracted the expected probability distribution function and the angular power spectrum of string-induced CMB temperature anisotropies up to $\ell \simeq 10^4$, including estimates of the systematic and statistical errors associated with our numerical simulations. Both of them exhibit distinctive features. In particular, strings should induce deviations from Gaussianity due to rare high temperature fluctuations, and lead to a power spectrum slowly decaying with increasing multipoles according to Eq. (14). Unless GU is well below the inflationary scale, the string-induced fluctuations start dominating the primary anisotropies for $\ell > \ell_{\text{min}}$, with $\ell_{\text{min}} \leq 10^4$. However, for values of GU smaller than a few times 10^{-7} , the string-induced anisotropies are themselves dominated by the tSZ, OV and nonlinear kSZ signals.

We also discussed the observability of strings in a typical arcminute-resolution experiment, focusing mainly on maps of the temperature gradient magnitude. Including the SZ effects in addition to the currently favored ΛCDM temperature anisotropies in our analysis, we find strings to be “eye visible,” in the sense that at least of order ten string features are observable on a 7.2° gradient map, for GU down to 2×10^{-7} . As already mentioned, a drawback in our study is that we do not include the effect of point sources. The main risk associated with point sources could actually be in their removal from CMB maps. Indeed, for values of GU lower than 2×10^{-7} , the gradient maps no longer show the typical linelike shape of strings but still contain rare high temperature fluctuations coming from the active string regions. Since the latter are localized, they may look like standard point sources, which could lead to their exclusion from CMB maps during the point-source removal process. A potential disambiguation method might rely on the intrinsic dipolar signature of these active string regions in the CMB temperature maps. Finally, let us mention that being able to take the gradient of a real temperature map requires a very good understanding of its noise properties, which could limit the applicability of the gradient technique described in this paper.

In addition to the statistical analyses we discussed at the end of Sec. IV C, other extensions of the present work might be worth thinking of. In particular, one might want to generate polarization maps, and especially their B-mode component since they have been shown to be string tracers [16, 91]. Some of the results presented here

may also be relevant to the production of gravitational waves by cosmic strings. The presence of cusps is indeed expected to trigger gravitational wave bursts. Since they also lay on our past light cone, their number is certainly related to the number of bright dipoles one may observe in our simulated maps.

Acknowledgments

The authors would like to thank Beth Reid and Hy Trac for their help in computing the tSZ, OV, and kSZ power spectra. C.R. benefited from the hospitality of the Department of Astrophysical Sciences at Princeton University, where this work was originated, and A.A.F. from a visit to Louvain University, where the final stages of this work were completed. The

cosmic string simulations have been performed thanks to computing support provided by the “Institut du Développement des Ressources en Informatique Scientifique” (<http://www.idris.fr>) and the Planck-HFI processing center at the Institut d’Astrophysique de Paris. A.A.F. acknowledges support from Princeton University, NASA Astrophysics Theory Program Grant No. NNG04GK55G, and NSF Program in International Research and Education Grant No. OISE-0530095. This work was also partially supported by the Belgian Federal Office for Scientific, Technical, and Cultural Affairs through the Inter-University Attraction Pole Grant No. P6/11. We acknowledge the use of the Legacy Archive for Microwave Background Analysis (LAMBDA). Support for LAMBDA is provided by the NASA Office of Space Science.

[1] S. Weinberg, *Rev. Mod. Phys.* **52**, 515 (1980).

[2] D. Kirzhnits and A. Linde, *Phys. Lett. B* **42**, 471 (1972).

[3] T. W. B. Kibble, *J. Phys. A* **9**, 1387 (1976).

[4] R. Jeannerot, J. Rocher, and M. Sakellariadou, *Phys. Rev. D* **68**, 103514 (2003), arXiv:hep-ph/0308134.

[5] R. Durrer, M. Kunz, and A. Melchiorri, *Phys. Rep.* **364**, 1 (2002), arXiv:astro-ph/0110348.

[6] A. Albrecht, R. A. Battye, and J. Robinson, *Phys. Rev. Lett.* **79**, 4736 (1997), arXiv:astro-ph/9707129.

[7] D. N. Spergel *et al.*, *Astrophys. J. Suppl. Ser.* **170**, 377 (2007), arXiv:astro-ph/0603449.

[8] A.-C. Davis and T. Kibble, *Contemp. Phys.* **46**, 313 (2005), arXiv:hep-th/0505050.

[9] N. Kaiser and A. Stebbins, *Nature (London)* **310**, 391 (1984).

[10] J. R. Gott III, *Astrophys. J.* **288**, 422 (1985).

[11] A. Vilenkin, *Phys. Lett. B* **107**, 47 (1981).

[12] T. Damour and A. Vilenkin, *Phys. Rev. D* **64**, 064008 (2001), arXiv:gr-qc/0104026.

[13] X. Siemens, J. Creighton, I. Maor, S. R. Majumder, K. Cannon, and J. Read, *Phys. Rev. D* **73**, 105001 (2006), arXiv:gr-qc/0603115.

[14] F. Bernardeau and J.-P. Uzan, *Phys. Rev. D* **63**, 023005 (2000), arXiv:astro-ph/0004102.

[15] M. Oguri and K. Takahashi, *Phys. Rev. D* **72**, 085013 (2005), arXiv:astro-ph/0509187.

[16] U. Seljak and A. Slosar, *Phys. Rev. D* **74**, 063523 (2006), arXiv:astro-ph/0604143.

[17] M. Wyman, L. Pogosian, and I. Wasserman, *Phys. Rev. D* **72**, 023513 (2005), arXiv:astro-ph/0503364.

[18] A. A. Fraisse, *J. Cosmol. Astropart. Phys.* **03**, 008 (2007), arXiv:astro-ph/0603589.

[19] N. Bevis, M. Hindmarsh, M. Kunz, and J. Urrestilla, *Phys. Rev. D* **75**, 065015 (2007), arXiv:astro-ph/0605018.

[20] D. P. Bennett and F. R. Bouchet, *Phys. Rev. Lett.* **63**, 2776 (1989).

[21] A. Albrecht and N. Turok, *Phys. Rev. D* **40**, 973 (1989).

[22] D. P. Bennett and F. R. Bouchet, *Phys. Rev. D* **41**, 2408 (1990).

[23] B. Allen and P. Shellard, *Phys. Rev. Lett.* **64**, 119 (1990).

[24] G. Vincent, N. D. Antunes, and M. Hindmarsh, *Phys. Rev. Lett.* **80**, 2277 (1998), arXiv:hep-ph/9708427.

[25] J. N. Moore, E. P. S. Shellard, and C. J. A. P. Martins, *Phys. Rev. D* **65**, 023503 (2001), arXiv:hep-ph/0107171.

[26] V. Vanchurin, K. Olum, and A. Vilenkin, *Phys. Rev. D* **72**, 063514 (2005), arXiv:gr-qc/0501040.

[27] C. J. A. P. Martins and E. P. S. Shellard, *Phys. Rev. D* **73**, 043515 (2006), arXiv:astro-ph/0511792.

[28] C. Ringeval, M. Sakellariadou, and F. R. Bouchet, *J. Cosmol. Astropart. Phys.* **02**, 023 (2007), arXiv:astro-ph/0511646.

[29] E. Jeong and G. F. Smoot, *Astrophys. J. Lett.* **661**, L1 (2007), arXiv:astro-ph/0612706.

[30] R. Barker *et al.* (AMII Collaboration), *Mon. Not. R. Astron. Soc.* **369**, L1 (2006), arXiv:astro-ph/0509215.

[31] J. Ruhl *et al.*, in *Millimeter and Submillimeter Detectors for Astronomy II*, edited by J. Zmuidzinas, W. S. Holland, and S. Withington (2004), vol. 5498 of *Proceedings of the SPIE*, p. 11, arXiv:astro-ph/0411122.

[32] A. Kosowsky, *New Astron. Rev.* **50**, 969 (2006).

[33] F. R. Bouchet, D. P. Bennett, and A. Stebbins, *Nature (London)* **335**, 410 (1988).

[34] M. Hindmarsh, *Nucl. Phys. B, Proc. Suppl.* **43**, 50 (1995), arXiv:astro-ph/9412079.

[35] U.-L. Pen, U. Seljak, and N. Turok, *Phys. Rev. Lett.* **79**, 1611 (1997), arXiv:astro-ph/9704165.

[36] R. Durrer, A. Gangui, and M. Sakellariadou, *Phys. Rev. Lett.* **76**, 579 (1996), arXiv:astro-ph/9507035.

[37] R. Durrer and Z.-H. Zhou, *Phys. Rev. D* **53**, 5394 (1996), arXiv:astro-ph/9508016.

[38] A. Albrecht, R. A. Battye, and J. Robinson, *Phys. Rev. D* **59**, 023508 (1998), arXiv:astro-ph/9711121.

[39] L. Pogosian and T. Vachaspati, *Phys. Rev. D* **60**, 083504 (1999), arXiv:astro-ph/9903361.

[40] J. Magueijo, A. Albrecht, P. Ferreira, and D. Coulson, *Phys. Rev. D* **54**, 3727 (1996), arXiv:astro-ph/9605047.

[41] R. Durrer, M. Kunz, and A. Melchiorri, *Phys. Rev. D* **59**, 123005 (1999), arXiv:astro-ph/9811174.

[42] C. Contaldi, M. Hindmarsh, and J. Magueijo, *Phys. Rev. Lett.* **82**, 679 (1999), arXiv:astro-ph/9808201.

[43] J.-H. P. Wu, P. P. Avelino, E. P. S. Shellard, and

B. Allen, Int. J. Mod. Phys. D **11**, 61 (2002), arXiv:astro-ph/9812156.

[44] N. Bevis, M. Hindmarsh, and M. Kunz, Phys. Rev. D **70**, 043508 (2004), arXiv:astro-ph/0403029.

[45] U.-L. Pen, D. N. Spergel, and N. Turok, Phys. Rev. D **49**, 692 (1994).

[46] B. Allen, R. R. Caldwell, S. Dodelson, L. Knox, E. P. S. Shellard, and A. Stebbins, Phys. Rev. Lett. **79**, 2624 (1997), arXiv:astro-ph/9704160.

[47] M. Landriau and E. P. S. Shellard, Phys. Rev. D **67**, 103512 (2003), arXiv:astro-ph/0208540.

[48] M. Landriau and E. P. S. Shellard, Phys. Rev. D **69**, 023003 (2004), arXiv:astro-ph/0302166.

[49] D. P. Bennett, A. Stebbins, and F. R. Bouchet, Astrophys. J. Lett. **399**, L5 (1992), arXiv:hep-ph/9206233.

[50] S. Dodelson, *Modern Cosmology* (Academic Press, Amsterdam, Netherlands, 2003).

[51] P. Peter and J.-P. Uzan, *Cosmologie primordiale* (Éditions Belin, Paris, France, 2005).

[52] J. M. Bardeen, Phys. Rev. D **22**, 1882 (1980).

[53] J. Silk, Astrophys. J. **151**, 459 (1968).

[54] R. Sachs and A. Wolfe, Astrophys. J. **147**, 73 (1967).

[55] A. Vilenkin and E. P. S. Shellard, *Cosmic Strings and Other Topological Defects* (Cambridge University Press, Cambridge, England, 2000).

[56] M. Hindmarsh, Astrophys. J. **431**, 534 (1994), arXiv:astro-ph/9307040.

[57] A. Stebbins and S. Veeraraghavan, Phys. Rev. D **51**, 1465 (1995), arXiv:astro-ph/9406067.

[58] A. Stebbins, Astrophys. J. **327**, 584 (1988).

[59] T. Vachaspati and A. Vilenkin, Phys. Rev. D **30**, 2036 (1984).

[60] V. Vanchurin, K. D. Olum, and A. Vilenkin, Phys. Rev. D **74**, 063527 (2006), arXiv:gr-qc/0511159.

[61] K. D. Olum and V. Vanchurin, Phys. Rev. D **75**, 063521 (2007), arXiv:astro-ph/0610419.

[62] C. J. A. P. Martins and E. P. S. Shellard, Phys. Rev. D **54**, 2535 (1996), arXiv:hep-ph/9602271.

[63] C. J. A. P. Martins and E. P. S. Shellard, Phys. Rev. D **65**, 043514 (2002), arXiv:hep-ph/0003298.

[64] M. White, J. Carlstrom, M. Dragovan, and W. Holzapfel, Astrophys. J. **514**, 12 (1999), arXiv:astro-ph/9712195.

[65] K. R. Mecke, T. Buchert, and H. Wagner, Astron. Astrophys. **288**, 697 (1994), arXiv:astro-ph/9312028.

[66] M. Hobson, A. Jones, and A. Lasenby, Mon. Not. R. Astron. Soc. **309**, 125 (1999), arXiv:astro-ph/9810200.

[67] E. Komatsu *et al.*, Astrophys. J. Suppl. Ser. **148**, 119 (2003), arXiv:astro-ph/0302223.

[68] T. Sousbie, C. Pichon, S. Colombi, D. Novikov, and D. Pogosyan, Mon. Not. R. Astron. Soc. **383**, 1655 (2008), arXiv:0707.3123.

[69] J. R. Gott III, C. Park, R. Juszkiewicz, W. E. Bies, D. P. Bennett, F. R. Bouchet, and A. Stebbins, Astrophys. J. **352**, 1 (1990).

[70] R. A. Sunyaev and Y. B. Zeldovich, Astrophys. Space Sci. **7**, 3 (1970).

[71] R. A. Sunyaev and Y. B. Zeldovich, Comments Astrophys. Space Phys. **4**, 173 (1972).

[72] E. Komatsu and U. Seljak, Mon. Not. R. Astron. Soc. **336**, 1256 (2002), arXiv:astro-ph/0205468.

[73] A. Jenkins, C. S. Frenk, S. D. M. White, J. M. Colberg, S. Cole, A. E. Evrard, H. M. P. Couchman, and N. Yoshida, Mon. Not. R. Astron. Soc. **321**, 372 (2001), arXiv:astro-ph/0005260.

[74] A. Lewis, A. Challinor, and A. Lasenby, Astrophys. J. **538**, 473 (2000), arXiv:astro-ph/9911177.

[75] E. Komatsu and T. Kitayama, Astrophys. J. Lett. **526**, L1 (1999), arXiv:astro-ph/9908087.

[76] R. A. Sunyaev and I. B. Zeldovich, Mon. Not. R. Astron. Soc. **190**, 413 (1980).

[77] J. P. Ostriker and E. T. Vishniac, Astrophys. J. Lett. **306**, L51 (1986).

[78] E. T. Vishniac, Astrophys. J. **322**, 597 (1987).

[79] W. Hu, Astrophys. J. **529**, 12 (2000), arXiv:astro-ph/9907103.

[80] C.-P. Ma and J. N. Fry, Phys. Rev. Lett. **88**, 211301 (2002), arXiv:astro-ph/0106342.

[81] P. Zhang, U.-L. Pen, and H. Trac, Mon. Not. R. Astron. Soc. **347**, 1224 (2004), arXiv:astro-ph/0304534.

[82] W. Hu and S. Dodelson, Annu. Rev. Astron. Astrophys. **40**, 171 (2002), arXiv:astro-ph/0110414.

[83] M. G. Santos, A. Cooray, Z. Haiman, L. Knox, and C.-P. Ma, Astrophys. J. **598**, 756 (2003), arXiv:astro-ph/0305471.

[84] M. McQuinn, S. R. Furlanetto, L. Hernquist, O. Zahn, and M. Zaldarriaga, Astrophys. J. **630**, 643 (2005), arXiv:astro-ph/0504189.

[85] I. Iliev, U.-L. Pen, J. Bond, G. Mellema, and P. Shapiro, Astrophys. J. **660**, 933 (2007), arXiv:astro-ph/0609592.

[86] K. M. Huffenberger and U. Seljak, New Astron. Rev. **10**, 491 (2005), arXiv:astro-ph/0408066.

[87] U. Seljak, A. Slosar, and P. McDonald, J. Cosmol. Astropart. Phys. **10**, 014 (2006), arXiv:astro-ph/0604335.

[88] N. Bevis, M. Hindmarsh, M. Kunz, and J. Urrestilla, Phys. Rev. Lett. **100**, 021301 (2008).

[89] T. A. Marriage, Ph.D. thesis, Princeton (2006).

[90] G. Rocha, M. P. Hobson, S. Smith, P. Ferreira, and A. Challinor, Mon. Not. R. Astron. Soc. **357**, 1 (2005), arXiv:astro-ph/0406136.

[91] N. Bevis, M. Hindmarsh, M. Kunz, and J. Urrestilla, Phys. Rev. D **76**, 043005 (2007), arXiv:0704.3800.